

# Remote Sensing of Satellite Activity through Optical and Infrared Temporal Differential Spectrophotometry Informed by Analysis of Noise

**John Kielkopf and Frank O. Clark**

*University of Louisville*

**Wellesley Pereira**

*AFRL/RV*

## ABSTRACT

We report new ground-based observations of satellites and analysis with the goal of detecting physical activity of, or within, the satellite itself. Alexander Graham Bell reported an optical method of detecting modulation of a surface membrane by voice at a distance (A.G. Bell) in 1880 and patented the concept [1, 2]. Applying this technique to resident space objects has been discussed extensively by Spurbeck, et al. 2021 [3]. Slater et al. 2016 [4] have proposed a small satellite to do this from space. Clark, Hay, and Kielkopf have made extensive observations of external surfaces demonstrating that light scattered from surfaces can reveal physical motion inside of the surface, including electrical motors and even structural defects [5, 6]. We have used telescope of the type described by Azari and Ehrhorn, and others [7], to measure these effects from Earth-orbiting satellites using several techniques guided by a goal to optimize information gathered while minimizing noise from the atmosphere, instrumentation, or intrinsic photon statistics. Spectral bands were selected from the visible to the thermal infrared, and data were acquired for focused and defocused, spatially unresolved, satellites while precisely tracked, and while allowed to drift across a field. Change in the observed flux is a consequence not only of change in the satellite, but also in its illumination, its aspect to the observer, the transmission along the line of sight, and the detection system and tracking optics. These sources of noise are well known in optical, infrared, and radio astronomy and can be modeled and moderated with techniques developed for precision part-per-thousand photometry of stellar flux variability. Noise can also be suppressed and weak signals enhanced through temporal analysis that identifies outliers, periodicities, and correlations across the multidimensional database spanning time and spectrum. These data show the possibilities and limitations of these techniques and indicate how observations may be optimized to enable extraction of a new class of information about internal dynamics and properties of resident space objects.

## 1. THE NEAR-EARTH SPACE AWARENESS PROBLEM

There are some 25,000 artificial objects in orbit above the Earth [8], including 8,171 active and defunct spacecraft tracked by the U.S. Space Surveillance Network. Among these are several thousand operational satellites [9], and a rapidly growing number of Starlink satellites from SpaceX, numbering 1469 to date with a projection of 30,000 upon completion. The latter interfere with ground-based astronomy and add to the clutter obscuring those of concern. Discerning operational satellites, and intrinsic physical properties of those operational satellites, amongst all of these objects is difficult. The scope of the problem is illustrated by a dynamic website tracking the known ones in real time, illustrated in Fig. 1. We propose a distance-independent observational method of deriving intrinsic physical properties of satellites and debris, a method which will sort them into a discernible “normal sequence,” easily separating outliers which have no thermal control, or which change their temperature. This approach directly measures (with calibration) thermal mass of an observed satellite. It does not require the object to be spatially resolved, although it can provide additional information if this is the case. This technique complements and completes Ground-Based Electro-Optical Deep Space Surveillance (GEODSS) by providing internal intrinsic physical properties of satellites, whereas GEODSS provides surface reflection and position.

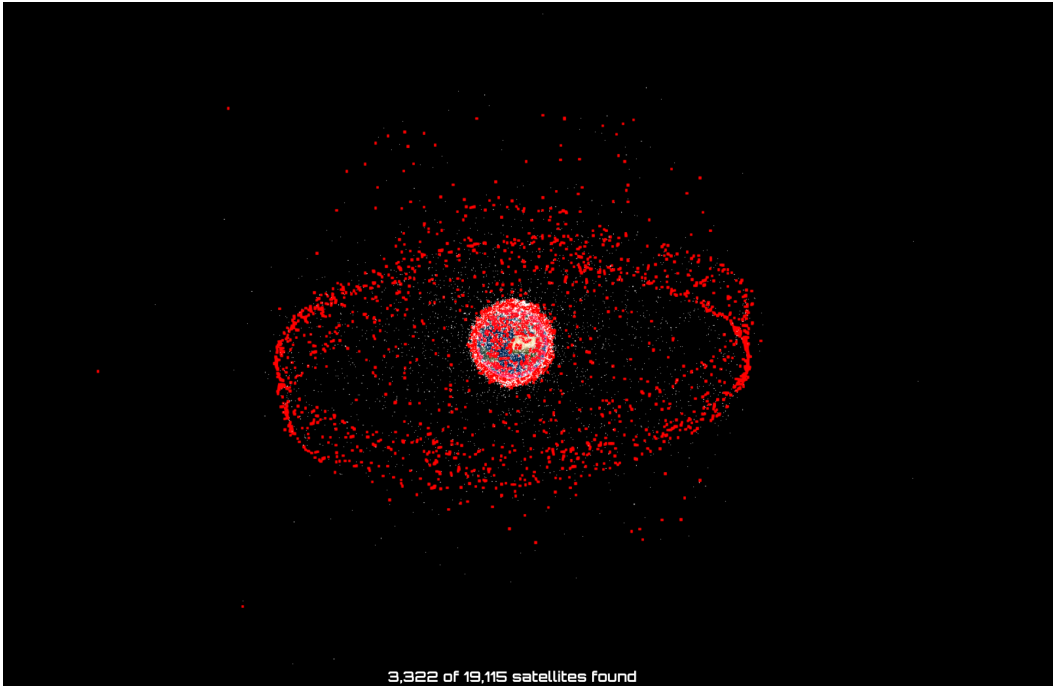


Fig. 1: A dynamic visualization of 19,115 satellites in Earth orbit on May 10, 2022 [10]. The satellites with a large radar cross-section are in red and scaled to enhance those in geosynchronous orbits.

## 2. GROUND-BASED TIME-SERIES PHOTOMETRY

Techniques of precision measurements of the flux from spatially unresolved astrophysical objects have been refined in the era of exoplanet searches dependent on detection of transit events in which a small fraction of the starlight is blocked by the obscuration by the planet's disk projected on the star. For a Jupiter-sized planet orbiting a solar-type star, this leads to a fractional light loss of the order of 10 parts per thousand, that is the square of the ratio of the planet to stellar radii, with allowance for the path of the planet across the disk and variations of stellar flux from limbdarkening and surface features. An example of the detection of a planet by this method in a ground-based observation of a TESS planet candidate is shown in Fig. 2. These measurements illustrate many of the factors that limit precision in photometry of point sources through Earth's atmosphere, while also demonstrating the part-per-thousand signal changes can be detected. The upper curve is relative flux for the target with respect to the other stars measured in the field. A relative measurement removes in large part the effects of varying transmission of Earth's atmosphere that is shown in the total comparison star count that is the lower curve of the figure. Those data are accompanied by a model of airmass and with it as a reference the remaining unpredictable changes in transparency are evident. It is not apparent here, but is a known factor, that the effects of transparency are color-dependent and the comparison stars have to be selected to match the color of the target in order to avoid systematic trends. The gray lowermost curve is sky brightness, rising toward dawn at the end of the data collection. Sky is not a major factor and is largely smoothly changing on a clear moonless night, but it contributes to noise through the excess photon count that must be subtracted in processing. The two middle curves show fitting a planet-transit model, the key to successful analysis, which does a multivariate fit allowing for the properties of the star, the planet, and the planet's orbit. This yields properties of the planet, e.g. its size relative to its host and the path of its orbit projected onto the face of the star. Three different binnings are shown in the data, and the noise is clearly reduced by co-adding data at the expense of time resolution.

On further inspection, the data from all 20 measured stars span a dynamic range of 1000 in flux and inform on how noise affects the measurement. This is illustrated in Fig. 3 which shows the signal in digital units (approximately 1 per photon detected) and the corresponding RMS noise relative to the signal in parts per thousand (PPT). The figure

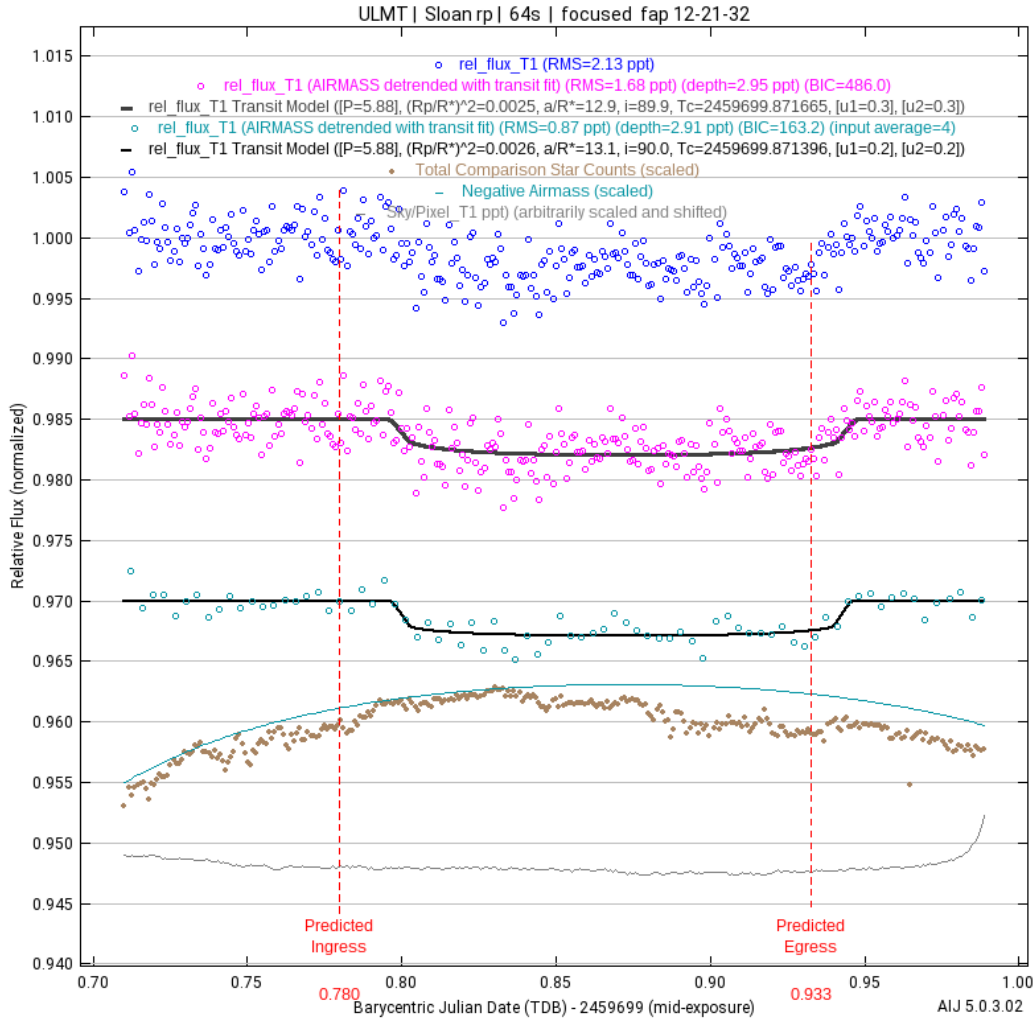


Fig. 2: An analysis of a time-series observation of a TESS transiting planet candidate from 311 images with 64-second exposures spanning 401 minutes with a 0.6 meter telescope on Mt. Lemmon. The target star is 11.6 V magnitude, and it was measured along with 19 other field stars for comparisons. The data were taken in a Sloan "r" (red) filter, and processed with AstroImageJ [11].

illustrates the factors that affect noise and enter into the "model" shown in the graph, along with a square-root Poisson distribution noise that would be present from photon statistics [12]. The noise model is a fit to a simplified form of the realistic model for point sources developed by Merline and Howell [13]. As implemented in AstroImageJ by Collins et al [11], it approaches the Poisson distribution in the absence of seeing, instrumental, and analysis effects:

- Detector gain (photons/digital unit)
- Number of pixels in the photometric aperture
- Number of pixels in the background measurement aperture (usually an annulus)
- Sky flux
- Dark signal
- Detector read noise
- Noise due to digitization loss
- Total measured flux from the target

Not included here, the quantum efficiency of the detector and the transmission of the optical system and Earth's atmosphere determine the measured flux for a given source outside the atmosphere. There is also a significant noise from pointing jitter. For our data, that is less than 1 arcsecond RMS over the series of observations, but this is also several pixels on the detector. Relative response of individual pixels adds to noise when the image wanders on the detector. Consequently, for a star of the order of 12th magnitude, an exposure time of 64 seconds, sub-arcsecond tracking, and nearby reference stars to mitigate atmospheric transmission, precision of 1 part per thousand can be maintained for data collected over 400 minutes. When applied to Earth-orbiting satellites, time-series data reveal changes in reflectivity (visible and near-infrared) and emissivity (thermal infrared) that inform on unresolved characteristics of the target. The limited window of observation of LEO satellites and their changing distance over the a sequence means that only short period changes are detectable in a single data collection, and that comparisons from one collection to another would be needed to detect longer period events. GEO satellites, by contrast, can be observed for hours with no or minimal tracking requirements and precision limited by atmospheric, instrumentation, and flux as indicated in this analysis of stellar data.

### 3. SPECTROPHOTOMETRIC COLOR

To mitigate the effect of changing distance, and to open another window onto the properties of satellites through spectrophotometry, the approach which motivates this study is to apply to Earth orbiting satellites an analog of a technique used in astrophysics for about a century to categorize stars by color-color measurements, which are distance independent. Reflected flux depends on materials and aging, and thermal radiation emitted depends on equilibrium temperature as well as heat capacity (thermal mass). Depending on its temperature, each satellite exhibits thermal emission that approximately corresponds to "black-body" radiation. The range of such satellite temperatures is well modeled and well measured. The spectral energy distribution exhibits an emission peak that shifts towards longer wavelengths for cooler temperatures and towards shorter wavelengths for warmer emission. The basic physics of determining this temperature remotely involves spectrophotometric imaging of the objects of interest using three or more "color bands" that cover the range of peak black-body emission that occurs under Earth orbital conditions. While increasing distance diminishes the observed flux in each band, its affect is the same on all of them. Thus color of an object, as defined by the ratio of energy flux at two wavelengths, intrinsically depends only on the physical properties of the object observed, not on its distance. By taking the flux ratios of pairs from a set of at least three bands, much as is done in astrophysical photometry, one may obtain a color-color plot [14]. The precise stellar analogs to what is proposed here are the photometric color-color comparisons of fluxes measured in the ultraviolet, blue, green/visible, red and infrared. A graph relating these observable colors displays a form of the stellar "main sequence" in which each object has a unique place correlated to its temperature. We show an example for stars measured with bands chosen for the Sloan Digital Sky Survey [15] in Fig. 4. For Earth-orbiting objects, determination of the wavelength of the peak emission in the long-wave or thermal infrared determines the temperature of the object, independent of distance.

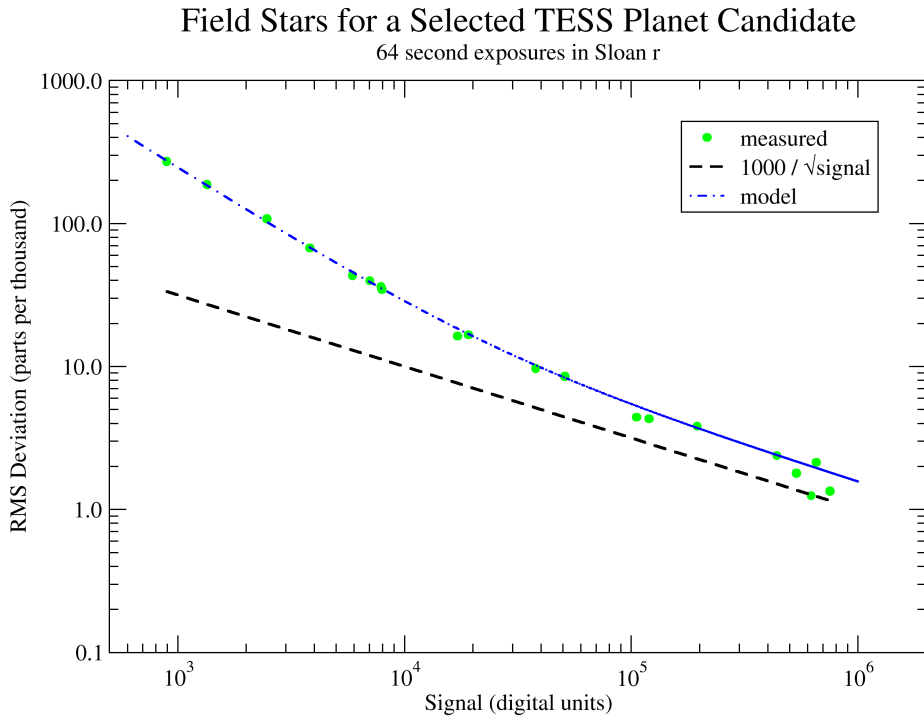


Fig. 3: Noise versus signal for the star and its comparisons in the data of Fig. 2. The lower dashed curve is a simple square root Poisson statistic noise that should be the best possible signal-noise ratio, while the upper curve is a noise model that includes factors known to affect photometry.

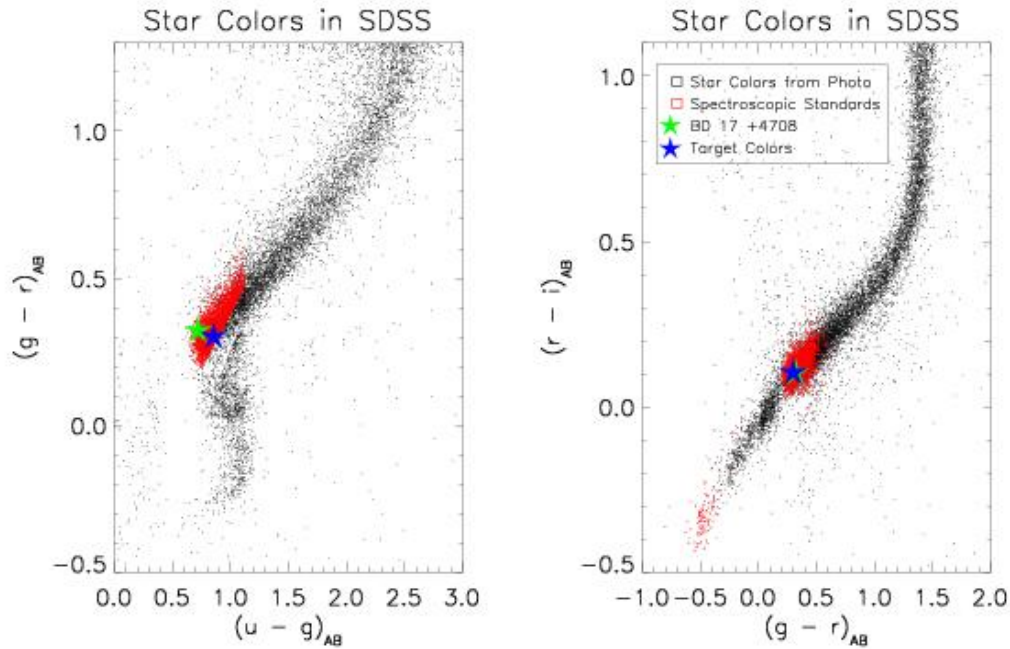


Fig. 4: Color-color diagrams for stars in the Sloan Digital Sky Survey. Positive values indicate greater flux at longer wavelengths. The standard Sloan filters are u, g, r, i, and z from the ultraviolet to the infrared [16]. These bands are paired such that the differences in magnitude (ratios of fluxes) are in separate spectral regions defining colors. The monotonic relationship is a dependence on effective temperature with hotter stars at the lower left [15]

That temperature is defined by radiative thermal equilibrium in space driven by the solar insolation primarily at visible and near-infrared wavelengths, its scattering back into space and absorption by the object, and the re-emission of this energy as thermal black-body radiation. The change in the temperature resulting from internal sources or from solar insolation depends in first order on the total mass of the object in question.

Figure 5 shows data from the Sloan Digital Sky Survey with magnitudes of main-belt asteroids measured in their filter system. The upper right panel isolates asteroids that are bluer (lower left) from those that are redder (upper right) in that plot, and the blue asteroids are associated with carbonaceous types, while the redder class is associated with silicate or rocky types [17]. The difference in asteroid spectral energy distributions is a consequence of strong absorption features in their reflected light that alter the flux in these bands, and change the magnitude differences. This example shows clearly how surface composition alters the distribution in a color-color analysis. The spectral properties of satellite materials and the debris that would come in the event of collision are being studied in a NASA DebrisSat program to find the optical characterization satellite fragments in support of orbital debris environmental models [18]. Thus there is a growing database of the expected optical properties of materials used in satellite construction, and the visible and near-infrared colors as seen from the ground will not depend on prior knowledge of the satellite's distance.

#### 4. DIFFERENTIATING GEO SATELLITES

As a test of these ideas in the optical and near-infrared, we observed a sample of geosynchronous satellites with a 0.6 meter telescope on Mt. Lemmon in Arizona. The telescope is Ritchie-Chrétien with a  $4K \times 4K$  CCD camera and filterwheel, and is a production version of a 0.5 meter prototype that was developed intentionally for satellite tracking [7], except that this one has an equatorial fork mount and is controlled by Sidereal Technology [19] motion controller and code that is capable of LEO tracking as well as astronomical tracking. The satellites that were observed were located using two-line elements (TLE) and the Python SkyField [20] code which, with a TLE for that epoch, predicted

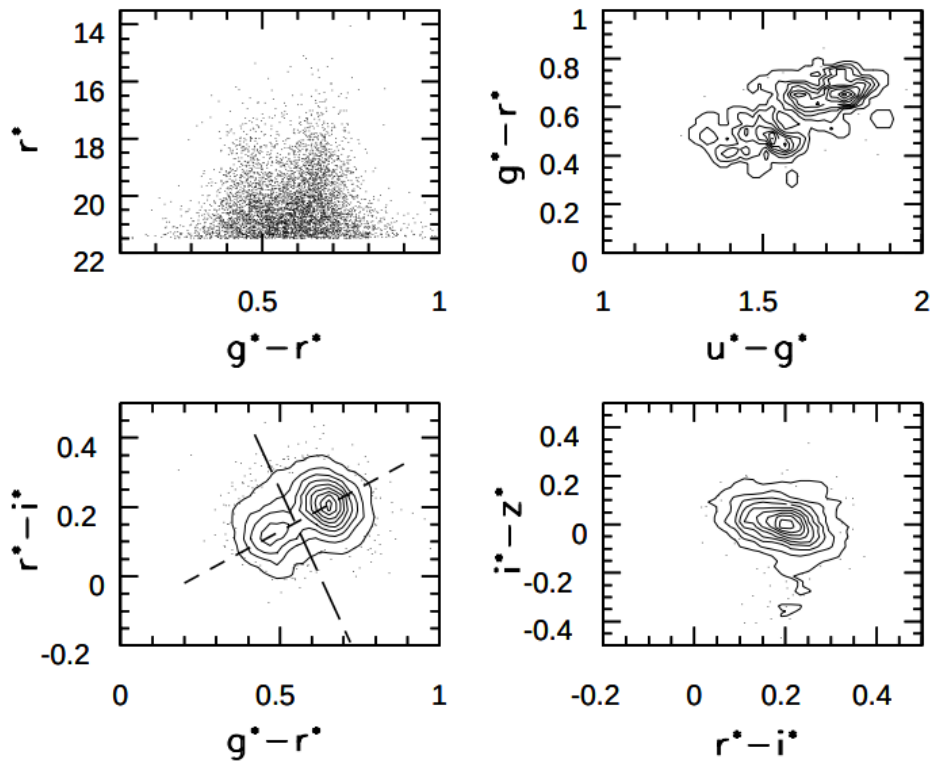


Fig. 5: Color-magnitude and color-color diagrams for 6150 main-belt asteroids. The color-color distribution is bimodal and a consequence of the band structure of materials and its effect on the spectrum of reflected light [17]. In the optical and near-infrared regions, material properties determine the relative colors.

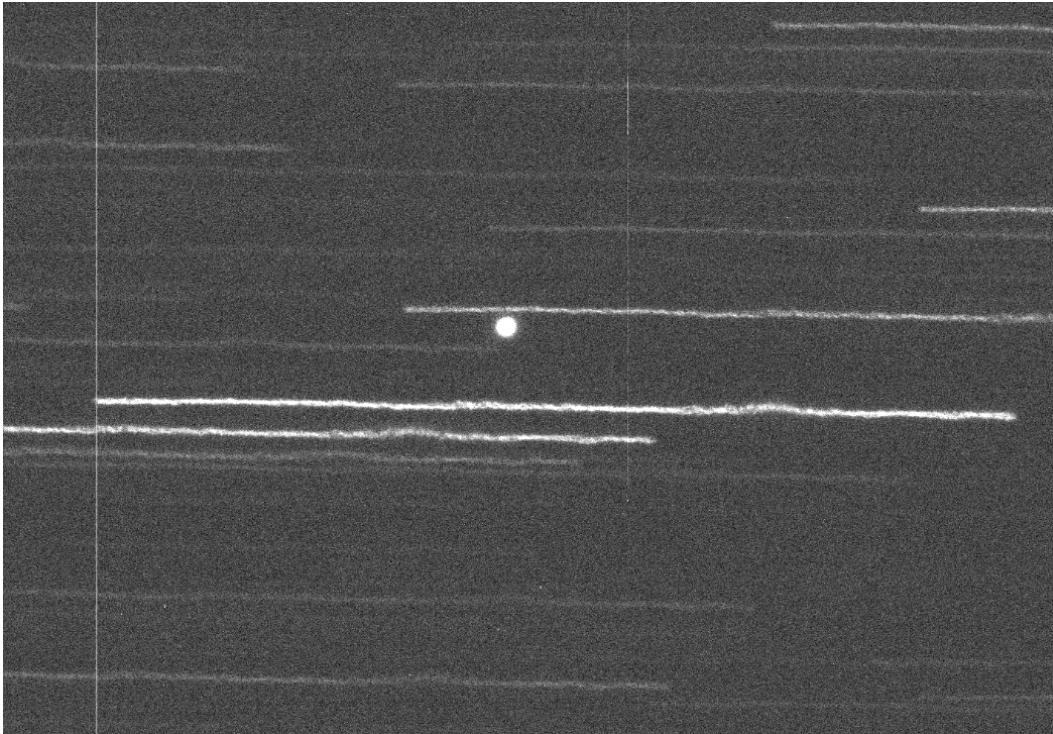


Fig. 6: A field surrounding GOES 16 for a 32 second exposure in Sloan r. The stars trail, and the GEO satellite is fixed because the telescope is parked at fixed altitude and azimuth. The star trails show the variation of atmospheric refraction responsible for seeing as they move at approximately 15 arcseconds/second in right ascension. Conversely, tracking at the sidereal rate trails the satellite, and its position is measured from the end of its trail at the moment of the the end of the exposure.

positions within a few arcseconds at the time of observation. This approach also insured identification of the satellite since in some cases several GEO satellites were in the same 0.5 degree field of the telescope.

An image of GOES-16 is shown in Fig.6 of an exposure in the Sloan r band with the telescope stationary and pointed at the satellite. The deviations in the stellar tracks from a perfect curve are due to atmospheric turbulence. To acquire an image of this type the telescope is pointed at the position the satellite is predicted to be in at a future time and it tracks at the sidereal rate at that virtual target. At the instant the satellite is predicted to be at the target location, the sidereal tracking is stopped and the exposure is started. Subsequently other filters are used to acquire a set of data in the Sloan g, r, i and z bands extending to the limit of the sensor's response in the near infrared. This type of exposure does not allow for flux calibration comparison stars in the same image, but these may be taken either before or after the collection of satellite data. The position of the satellite is measured by taking an exposure with sidereal tracking and measuring the position of the GEO satellite from terminus of its apparent motion at the end of the exposure.

Integrated flux with sky subtraction in each band was determined by aperture photometry and corrected for the telescope's relative response in each filter. The telescope response function was found by measuring a 109 Vir, a flux standard star with "0" Johnson-Cousins colors and for which a thermal blackbody calibration has been made [21]. There is a physical standard behind the assignment of color. The data thus yield pairs of measurements: g-r, r-i, i-z on the magnitude scale. That is, these magnitude differences are proportional to the log of the flux ratios in the band pairs and are set to zero for an A0 type star that is the astronomical "white" star. The resulting data can be analyzed in a 3D color-color plot that allows for projection onto the planes that are the conventional color-color 2D plots. Alternatively, color may be correlated with any other distance-independent property. An interactive 3D plot is informative about the characteristics different satellites have in common, as expected. Data on 7 satellites (GOES 14-18, SGDC, and Star One) are shown in 7.

## GEO Satellites Color-Color Relationship

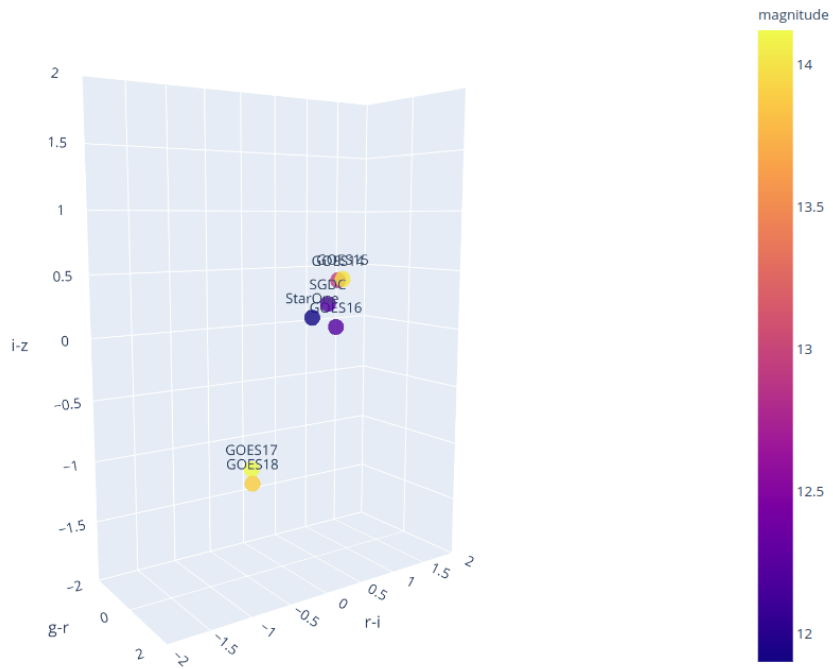


Fig. 7: Colors of satellites in the Sloan filter bands given as differences  $g-r$ ,  $r-i$ , and  $i-z$  are shown in a static view of a dynamic 3D plot. On the magnitude scale a larger number is fainter. A color value of 0 is neutral with equal flux in the short and longer wavelength bands. A negative color means the longer wavelength band has lower flux and a larger magnitude than the short wavelength one it is compared to. Conversely, large color values mean that the flux is increasing toward longer, redder, wavelengths. A fourth dimension of magnitude is added by color-coding. All of the satellites are nominally at the same distance and therefore magnitude or flux comparisons are also useful for correlating characteristics. The two lowermost satellites are GOES 17 and 18, the most recently launched of the series. The grouping on the upper right of colors includes the oldest satellites, GOES 14 and 15, at the extreme. Two Brazilian satellites, Star One and SGDC, are in that group as well.

## Thermal Radiation Sources Space-Based Spectrophotometric Radiance

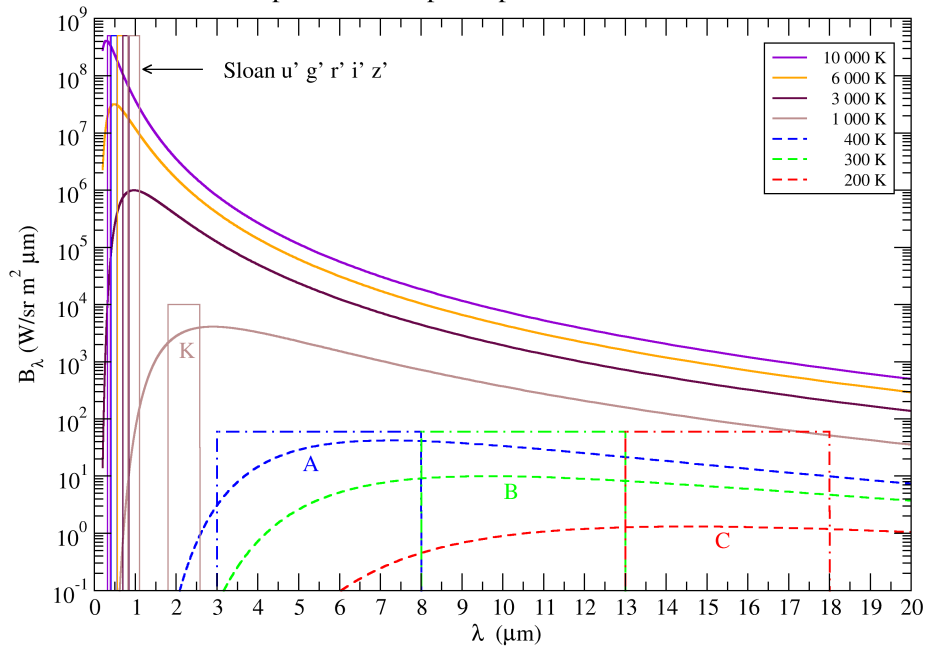


Fig. 8: The radiance of a thermal black-body source at 400 K, 300 K, and 200 K in the thermal infrared spectral region out to a wavelength of 20  $\mu\text{m}$ . Three filter bands are identified that isolate the maxima which shift with temperature. Also shown, the hotter sources typical of astrophysical observations have corresponding spectral bands suitable for measuring their temperatures also using color-color or color-magnitude relations.

The error bars for the colors are of the order of 0.01 magnitude, but with longer duration data and comprehensive calibration this can be reduced to 0.001, that is the PPT level that is possible for stellar photometry limited by atmospheric and tracking issues. That GEO satellites can be observed without active tracking and are bright enough for telescopes in the 0.5 meter class to follow routinely enabling long term monitoring and classification with simple schema, and the opportunity to learn about the information in long-period temporal signals. LEO satellites with their short transient passages, present a different technical challenge in calibration and precision, also with PPT level possible given fast response detectors with stable performance. Based on the noise analysis of data for transiting exoplanets, a critical factor is the pixel-to-pixel variations in sensitivity that add noise from image jitter.

### 5. COLORS IN THE THERMAL INFRARED

This method may be applied to the self-luminous radiation from Earth-orbiting satellites. Figure 8 shows the three wavelength bands required to cover the change in expected thermal black-body emission for objects in space at Earth's distance from the Sun in radiative equilibrium. Band A (3-8  $\mu\text{m}$ ), and band B (8-13  $\mu\text{m}$ ) may both be covered with conventional focal plane arrays, but an imaging sensor for band C (13-18  $\mu\text{m}$ ) is not available off the shelf and will require some focal plane development.

These three bands are a close analog to selected Johnson-Cousins filters designated U, B, V, R, and I designed in the days of photography to broadly sample the visible spectrum from the ultraviolet to the infrared [22]. The contemporary Sloan u, g, r, i, and z system filters [16, 23] along with infrared J, K, and L filters used in optical astronomy, cover the

## Thermal Source Radiance

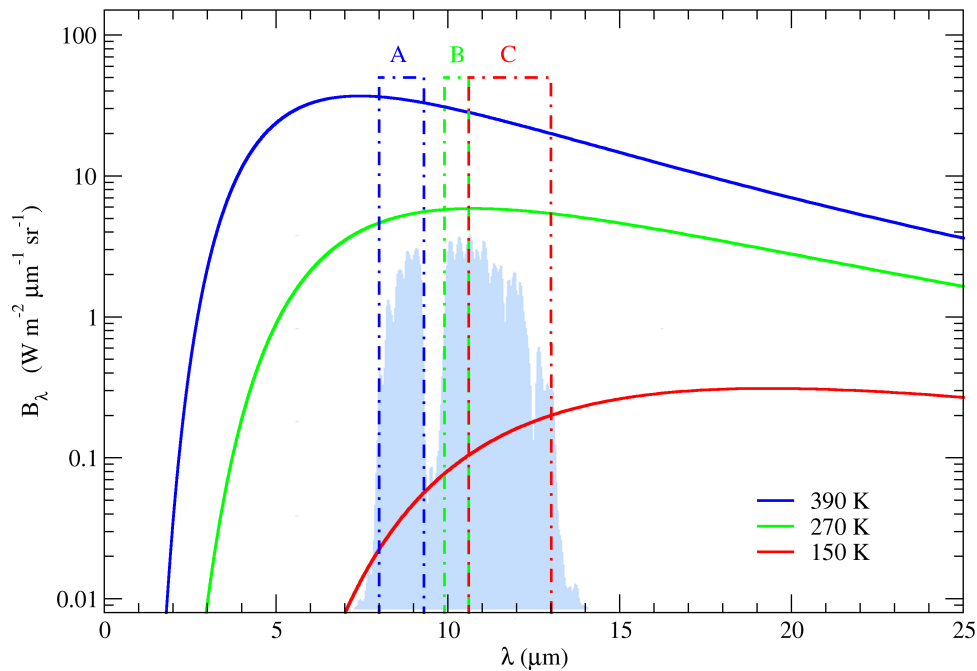


Fig. 9: From the Earth’s surface, long wavelength typical transmission of Earth’s atmosphere on a linear scale [24] overlays the passbands and detector response within an atmospheric window from 8 to 12 microns that provide data that discriminate the temperature of the source. The observable relative fluxes in a passband inform an infrared “color” of the object represented by the perfect black-body emission at temperatures typical of the range found in low-Earth orbit. Band A from 8.0 to 9.3  $\mu\text{m}$  begins at the lower bound of a microbolometer’s response and cuts at the edge of the atmospheric ozone absorption feature. Band B from 9.9 to 10.6  $\mu\text{m}$  collects from above the ozone feature to include the peak thermal emission of an object at nominal thermal equilibrium in low-Earth orbit. Band C from 10.6 to 13.0  $\mu\text{m}$  samples to the upper limit of a microbolometer’s response while integrating the peak of cooling objects out of solar insolation.

range of shift in the black-body peak for astronomical objects. In the case of stars, the opacity of their atmosphere also affects the colors, and a significant non-thermal Balmer decrement in opacity even informs on the composition and state of stellar photospheres. For the known range of Earth-orbiting satellite temperatures, the spectral characteristics of the materials also influence deviations from the perfect black body, informing on the composition and texture as well as the temperature. Such measurements in the thermal infrared, while best done from space where there is no intervening effect of Earth’s atmosphere, are amenable to ground based verification by choosing three suitable passbands within the 8-12 micron window excluding atmospheric ozone.

Figure 9 illustrates three such refined passbands within the 8-12  $\mu\text{m}$  window, at 8.0-9.3, 9.9-10.6, and 10.6-13.0  $\mu\text{m}$ . Alternatively, a low-resolution spectroscopic approach to this window would offer the greatest information return. Either would be sufficient for a proof of principal experiment and can be done from the ground because the atmosphere is largely transparent in this regime. Differential measurements distinguish the Earth orbiting source from the ambient and instrumental thermal emission background.

Relative measurements of radiative fluxes at three or more wavelengths, as shown for example in Figures 5 and 8, become “color,” and are distance independent, meaning that these three measurements made in the thermal emission

regime are alone sufficient to characterize radiative equilibrium of objects at that moment, be they stars, asteroids, or Earth satellites (this concept is University of Louisville proprietary). This is a stand-alone technique, rapidly cataloguing thermal properties, and yielding details about mass and temperature. When combined with traditional measurements of orbits, albedo, and rotation, additional knowledge is gained about the satellite [25, 26, 27, 28].

In analogy with the astronomical case, once calibrated, the observed satellite data in a color-color diagram using the three filters above should yield a “normal sequence” of satellites uniquely determining the temperature from a distance-independent measurement. Repeated observations and monitoring provide a time dependence of the temperature changes in response to variations in insolation and shadowing over the course of an orbit. The amplitude and phasing of the observed thermal response is determined by an object’s heat capacity and internal structure, that is, by its effective thermal mass. A Markov chain Monte Carlo analysis now commonly exploited in observational astrophysics data modeling produces not only our “equivalent Hertzsprung-Russell diagram” for thermal emission of satellites, determining their temperature, but aligns it with properties known for all satellites. However, in the case that such multi-dimensional analysis proves too time consuming, spectral data combined into into three equivalent “photometric bands” across the 8-12  $\mu\text{m}$  window designed to suppress the time-variable ozone feature will serve for three-color analysis.

## 6. CONCLUSION

Colors of satellites are distance-independent observable characteristics that distinguish satellites by age and structure. Part-per-thousand precision is possible in color and relative flux measurements as indicated by the achievements of contemporary ground-based astronomy in followup of discoveries by NASA’s Kepler and TESS satellites. With an appropriate detector, measurements in the thermal infrared can be made which would mitigate the variability of atmospheric transmission in the regions where typical thermal emission of satellites occurs.

## REFERENCES

- [1] A.G. Bell. “Selenium and the photophone”. In: *Nature* 22 (Sept. 1880), pp. 500–503.
- [2] A.G. Bell and S. Tainter. *Photophone Transmitter*. U.S. Patent 235496 issued December 14, 1880.
- [3] Justin Spurbeck et al. “Near Real Time Satellite Event Detection, Characterization, and Operational Assessment Via the Exploitation of Remote Photoacoustic Signatures”. In: *Journal of the Astronautical Sciences* 68.1 (Mar. 2021), pp. 197–224. DOI: [10.1007/s40295-021-00252-5](https://doi.org/10.1007/s40295-021-00252-5).
- [4] D. Slater et al. “Light to Sound: The Remote Acoustic Sensing Satellite (RASSat)”. In: vol. XI-05. Small Satellite Conference Series. 2016.
- [5] F.O. Clark. *Remote Passive Measurement of Information Including Engine Shaft Speed*. U.S. Patent 8284405, 2012.
- [6] J. Kielkopf and J. Hay. *System and Method for Precision Measurement of Position, Motion and Resonances*. U.S. Patent 8693735 issued April 8, 2014.
- [7] B. Ehrhorn and D. Azari. “Autonomous Low Earth Orbit Satellite and Orbital Debris Tracking Using Mid Aperture COTS Optical Trackers”. In: *Advanced Maui Optical and Space Surveillance Technologies Conference*. Ed. by S. Ryan. Jan. 2007, E10, E10.
- [8] NASA Orbital Debris Program Office. “Box Score”. In: *Orbital Debris Quarterly News* 26 (Mar. 2022), p. 10. URL: <https://orbitaldebris.jsc.nasa.gov/quarterly-news/pdfs/odqnv26i1.pdf>.
- [9] Union of Concerned Scientists. *Satellite Database*. 2022. URL: <https://www.ucsusa.org/resources/satellite-database> (visited on 05/10/2022).
- [10] ESRI. *Satellite Map*. 2022. URL: <https://geoxc-apps2.bd.esri.com/Visualization/sat2/index.html> (visited on 05/10/2022).
- [11] K. A. Collins et al. “AstroImageJ: Image Processing and Photometric Extraction for Ultra-precise Astronomical Light Curves”. In: *AJ* 153, 77 (Feb. 2017), p. 77. DOI: [10.3847/1538-3881/153/2/77](https://doi.org/10.3847/1538-3881/153/2/77). arXiv: [1701.04817](https://arxiv.org/abs/1701.04817) [astro-ph.IM].

- [12] D. L. Fried. “Noise in photoemission current”. In: *Applied Optics* 4 (1965), pp. 79–80.
- [13] W. J. Merline and Steve B. Howell. “A Realistic Model for Point-sources Imaged on Array Detectors: The Model and Initial Results”. In: *Experimental Astronomy* 6.1-2 (Jan. 1995), pp. 163–210. DOI: [10.1007/BF00421131](https://doi.org/10.1007/BF00421131).
- [14] Wikipedia. *Color-color diagram*. 2022. URL: [https://en.wikipedia.org/wiki/Color%E2%80%93color\\_diagram](https://en.wikipedia.org/wiki/Color%E2%80%93color_diagram) (visited on 05/10/2022).
- [15] Sloan Digital Sky Survey. *Star Colors*. 2022. URL: [https://www.sdss.org/stdstar\\_colors/](https://www.sdss.org/stdstar_colors/) (visited on 05/11/2022).
- [16] M. Fukugita et al. “The Sloan Digital Sky Survey Photometric System”. In: *AJ* 111 (Apr. 1996), p. 1748. DOI: [10.1086/117915](https://doi.org/10.1086/117915).
- [17] Željko Ivezić et al. “Solar System Objects Observed in the Sloan Digital Sky Survey Commissioning Data”. In: *AJ* 122.5 (Nov. 2001), pp. 2749–2784. DOI: [10.1086/323452](https://doi.org/10.1086/323452). arXiv: [astro-ph/0105511](https://arxiv.org/abs/astro-ph/0105511) [astro-ph].
- [18] Heather M. Cowardin et al. “Optical Characterization of DebrisSat Fragments in Support of Orbital Debris Environmental Models”. In: *Journal of the Astronautical Sciences* 68.4 (Dec. 2021), pp. 1186–1205. DOI: [10.1007/s40295-021-00278-9](https://doi.org/10.1007/s40295-021-00278-9).
- [19] D. Gray. *Sidereal Technology Force One*. 2022. URL: [http://siderealtechnology.com/BrushlessManual\\_1\\_4.pdf](http://siderealtechnology.com/BrushlessManual_1_4.pdf) (visited on 08/26/2022).
- [20] Brandon Rhodes. *Skyfield: High precision research-grade positions for planets and Earth satellites generator*. Astrophysics Source Code Library, record ascl:1907.024. July 2019. ascl: [1907.024](https://ascl.net/1907.024).
- [21] Charles W. Engelke, Stephan D. Price, and Kathleen E. Kraemer. “Spectral Irradiance Calibration in the Infrared. XVII. Zero-magnitude Broadband Flux Reference for Visible-to-infrared Photometry”. In: *AJ* 140.6 (Dec. 2010), pp. 1919–1928. DOI: [10.1088/0004-6256/140/6/1919](https://doi.org/10.1088/0004-6256/140/6/1919).
- [22] Michael S. Bessell. “Standard Photometric Systems”. In: *ARA&A* 43.1 (Sept. 2005), pp. 293–336. DOI: [10.1146/annurev.astro.41.082801.100251](https://doi.org/10.1146/annurev.astro.41.082801.100251).
- [23] Michael R. Blanton et al. “Sloan Digital Sky Survey IV: Mapping the Milky Way, Nearby Galaxies, and the Distant Universe”. In: *AJ* 154.1, 28 (July 2017), p. 28. DOI: [10.3847/1538-3881/aa7567](https://doi.org/10.3847/1538-3881/aa7567). arXiv: [1703.00052](https://arxiv.org/abs/1703.00052) [astro-ph.GA].
- [24] Spectral Sciences Inc. *Modtran*. 2022. URL: [http://modtran.spectral.com/modtran\\_home](http://modtran.spectral.com/modtran_home) (visited on 06/04/2022).
- [25] Tatsuaki Okada et al. “Highly porous nature of a primitive asteroid revealed by thermal imaging”. In: *Nature* 579.7800 (Mar. 2020), pp. 518–522. DOI: [10.1038/s41586-020-2102-6](https://doi.org/10.1038/s41586-020-2102-6).
- [26] A. Labibian et al. “Development of a radiation based heat model for satellite attitude determination”. In: *Aerospace Science and Technology* 82-83 (2018), pp. 479–486. ISSN: 1270-9638. DOI: <https://doi.org/10.1016/j.ast.2018.09.031>. URL: <https://www.sciencedirect.com/science/article/pii/S1270963818314159>.
- [27] Xiao-Fen Zhao et al. “Multicolor photometry of geosynchronous satellites and application on feature recognition”. In: *Advances in Space Research* 58.11 (Dec. 2016), pp. 2269–2279. DOI: [10.1016/j.asr.2016.09.020](https://doi.org/10.1016/j.asr.2016.09.020).
- [28] A. Vananti, T. Schildknecht, and H. Krag. “Reflectance spectroscopy characterization of space debris”. In: *Advances in Space Research* 59.10 (May 2017), pp. 2488–2500. DOI: [10.1016/j.asr.2017.02.033](https://doi.org/10.1016/j.asr.2017.02.033).